HHS Public Access

Author manuscript

Anal Chem. Author manuscript; available in PMC 2023 June 06.

Published in final edited form as:

Anal Chem. 2023 May 16; 95(19): 7665–7675. doi:10.1021/acs.analchem.3c00624.

Assessing Breast Cancer Molecular Subtypes Using Extracellular Vesicles' mRNA

Mengjia Hu,

Department of Cancer Biology, The University of Kansas Medical Center, Kansas City, Kansas 66160, United States; Center of BioModular Multi-Scale Systems for Precision Medicine and Department of Chemistry, The University of Kansas, Lawrence, Kansas 66045, United States; Kansas Institute for Precision Medicine, University of Kansas Medical Center, Kansas City, Kansas 66160, United States

Virginia Brown,

Center of BioModular Multi-Scale Systems for Precision Medicine and Bioengineering Program, The University of Kansas, Lawrence, Kansas 66045, United States

Joshua M. Jackson,

Center of BioModular Multi-Scale Systems for Precision Medicine and Department of Chemistry, The University of Kansas, Lawrence, Kansas 66045, United States

Harshani Wijerathne,

Center of BioModular Multi-Scale Systems for Precision Medicine and Department of Chemistry, The University of Kansas, Lawrence, Kansas 66045, United States

Harsh Pathak,

Department of Pathology and Laboratory Medicine and Kansas Institute for Precision Medicine, University of Kansas Medical Center, Kansas City, Kansas 66160, United States

Devin C. Koestler,

Kansas Institute for Precision Medicine, University of Kansas Medical Center, Kansas City, Kansas 66160, United States; Department of Biostatistics & Data Science, The University of Kansas Medical Center, Kansas City, Kansas 66160, United States

Corresponding Authors Malgorzata A. Witek – *Center of BioModular Multi-Scale Systems for Precision Medicine and Department of Chemistry, The University of Kansas, Lawrence, Kansas 66045, United States; Kansas Institute for Precision Medicine, University of Kansas Medical Center, Kansas City, Kansas 66160, United States*; mwitek@ku.edu; **Steven A. Soper** – *Department of Cancer Biology, The University of Kansas Medical Center, Kansas City, Kansas 66160, United States; Center of BioModular Multi-Scale Systems for Precision Medicine, Department of Chemistry, Bioengineering Program, and Department of Mechanical Engineering, The University of Kansas, Lawrence, Kansas 66045, United States; Kansas Institute for Precision Medicine, University of Kansas Medical Center, Kansas City, Kansas 66160, United States; BioFluidica, Inc., San Diego, California 92121, United States;* ssoper@ku.edu.

Author Contributions

M.H., V.B., and J.M.J. contributed equally. The manuscript was written through contributions of all authors, and all authors have given approval to the final version of the manuscript.

Supporting Information

The Supporting Information is available free of charge at https://pubs.acs.org/doi/10.1021/acs.analchem.3c00624.
Additional experimental details, materials, methods, supporting results, performance characteristics, parameters used for 3D COMSOL simulations, healthy donors enrolled in study, female breast cancer patients enrolled in study, summary of TRNA mass, correlation of transcript abundance, description of exo-mRNA transcripts, Spearman correlation coefficients, simulation results, Cy5 fluorescence microscopy images, protein content, primer designs, concentration and size distribution results, representative electropherograms, and heatmaps (PDF)

The authors declare the following competing financial interest(s): Technology reported in this manuscript is commercialized by BioFluidica Co. Some of the authors have equity in this company, including the corresponding author (Soper).

Emily Nissen,
Department of Biostatistics & Data Science, The University of Kansas Medical Center, Kansas City, Kansas 66160, United States

Mateusz L. Hupert,
BioFluidica, Inc., San Diego, California 92121, United States

Rolf Muller,
BioFluidica, Inc., San Diego, California 92121, United States

Andrew K. Godwin,
Center of BioModular Multi-Scale Systems for Precision Medicine, The University of Kansas, Lawrence, Kansas 66045, United States; Department of Pathology and Laboratory Medicine and Kansas Institute for Precision Medicine, University of Kansas Medical Center, Kansas City, Kansas 66160, United States

Malgorzata A. Witek,
Center of BioModular Multi-Scale Systems for Precision Medicine and Department of Chemistry, The University of Kansas, Lawrence, Kansas 66045, United States; Kansas Institute for Precision Medicine, University of Kansas Medical Center, Kansas City, Kansas 66160, United States

Steven A. Soper
Department of Cancer Biology, The University of Kansas Medical Center, Kansas City, Kansas 66160, United States; Center of BioModular Multi-Scale Systems for Precision Medicine, Department of Chemistry, Bioengineering Program, and Department of Mechanical Engineering, The University of Kansas, Lawrence, Kansas 66045, United States; Kansas Institute for Precision Medicine, University of Kansas Medical Center, Kansas City, Kansas 66160, United States; BioFluidica, Inc., San Diego, California 92121, United States

Abstract

Extracellular vesicles (EVs) carry RNA cargo that is believed to be associated with the cell-of-origin and thus have the potential to serve as a minimally invasive liquid biopsy marker for supplying molecular information to guide treatment decisions (i.e., precision medicine). We report the affinity isolation of EV subpopulations with monoclonal antibodies attached to the surface of a microfluidic chip that is made from a plastic to allow for high-scale production. The EV microfluidic affinity purification (EV-MAP) chip was used for the isolation of EVs sourced from two-orthogonal cell types and was demonstrated for its utility in a proof-of-concept application to provide molecular subtyping information for breast cancer patients. The orthogonal selection process better recapitulated the epithelial tumor microenvironment by isolating two subpopulations of EVs: EV^{EpCAM} (epithelial cell adhesion molecule, epithelial origin) and $EV^{FAP\alpha}$ (fibroblast activation protein α, mesenchymal origin). The EV-MAP provided recovery >80% with a specificity of 99 ± 1% based on exosomal mRNA (exo-mRNA) and real time–droplet digital polymerase chain reaction results. When selected from the plasma of healthy donors and breast cancer patients, EVs did not differ in size or total RNA mass for both markers. On average, 0.5 mL of plasma from breast cancer patients yielded ~2.25 ng of total RNA for both EV^{EpCAM} and $EV^{FAP\alpha}$, while in the case of cancer-free individuals, it yielded 0.8 and 1.25 ng of total RNA from EV^{EpCAM} and $EV^{FAP\alpha}$, respectively. To assess the potential of these two EV subpopulations

to provide molecular information for prognostication, we performed the PAM50 test (Prosigna) on exo-mRNA harvested from each EV subpopulation. Results suggested that EV^{EpCAM} and $EV^{EAP\alpha}$ exo-mRNA profiling using subsets of the PAM50 genes and a novel algorithm (i.e., exo-PAM50) generated 100% concordance with the tumor tissue.

Graphical Abstract

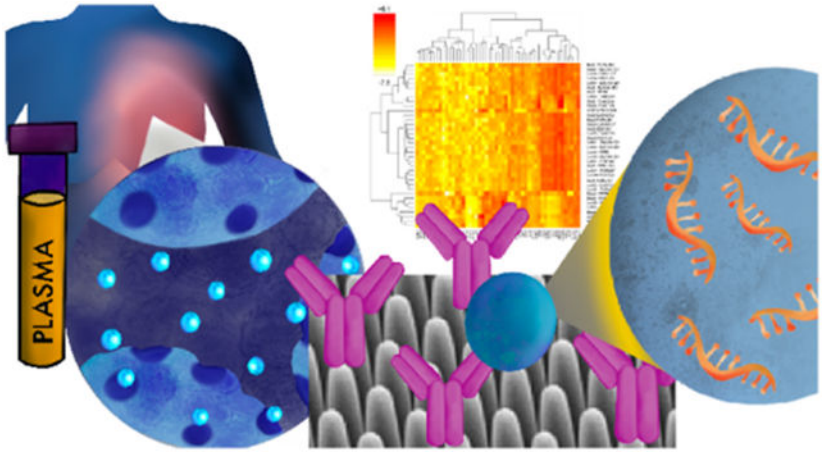

INTRODUCTION

One type of liquid biopsy marker for cancer disease management is extracellular vesicles (EVs), which can be found in relatively high abundance even for early-stage disease. EVs (i.e., exosomes, microvesicles, and apoptotic bodies) originate from cells via multivesicular endosome fusion with the cell membrane or membrane budding for exosomes and microvesicles, respectively. Both contain cargos that includes proteins, lipids, and nucleic acids.[1-4]

EV-associated ribonucleic acid (RNA) can reflect changes in the RNA expression of the cells from which they were generated.[5-7] However, the analysis of EV mRNA (exo-mRNA) is challenging due to the low abundance of these molecules in the pool of total RNA harvested from EVs including microRNA (miRNA), mRNA, ribosomal RNA (rRNA), and long noncoding RNA (lncRNA);[8] EVs can carry up to ~10,000 nt of nucleic acids.[9] While the packaging of RNAs[10-12] into EVs protects these molecules from RNase degradation, studies have found little or no full-length 18S or 28s rRNA in EVs.[13,14] Wei et al. reported that while exo-miRNA can make up ~42% of the total RNA content in EVs,[13] exo-mRNA comprises <2% of the total RNA content. Full-length mRNA transcripts were found in shedding microvesicles but not in exosomes with the EV RNA size ranging between 200 and 500 nt.[15] Few studies have reported exo-mRNA analysis most likely due to its low abundance in EVs.[16-21] In spite of the aforementioned limitation associated with exo-mRNA, there is an increased interest in the use of exo-mRNA analysis for cancer disease management. Different EV isolation methods have been used in combination with real-time quantitative reverse transcription polymerase chain reaction (RT-qPCR) or droplet digital PCR (ddPCR) to gather gene expression information of different cancers.[22-28]

Whatever type of molecular analysis is performed on EVs, disease-associated EVs must be enriched from complex biological samples, such as plasma, before analysis. Most methods for EV enrichment target all EVs irrespective of the cellular source. Therefore, low abundant mRNA transcripts whose expression alterations can serve as a disease indicator are "diluted" among the total RNAs carried by non-diseased EVs. This highlights the need for methods to specifically enrich disease-associated EVs in sufficient quantity and purity to evaluate the use of exo-mRNA as a disease biomarker.[29,30] The "gold standard" for EV isolation has been differential ultracentrifugation, a laborious method with poor analytical figures-of-merit.[31] Newer methods for EV isolation include polymer precipitation, ion exchange columns, ultrafiltration, and size-exclusion chromatography. The aforementioned enrichment techniques isolate all EVs irrespective of the cellular source.[31]

There have been reports on the use of microfluidics for the enrichment of EVs (see Table S1).[32,33] Microfluidics for EV isolation can be parsed into two categories: (i) selection via physical properties such as EV size or density and (ii) selection by biological properties, such as presentation of an antigenic marker for affinity enrichment. Microfluidics exploiting physical EV properties selects all EVs irrespective of the cell-of-origin. In cases requiring profiling exo-mRNA, the background produced by non-diseased exo-mRNAs can mask expression differences of tumor-derived exo-mRNA.[16]

Microfluidics with surface-attached mAbs that target pan-EV markers, such as the tetraspanins (CD63, CD81, or CD9), enriches exosomes irrespective of their cell-of-origin.[34-38] This approach can also mask disease signatures making disease-specific molecular profiling difficult. Targeting surface proteins that are disease-specific could obviate this problem. For example, several reports have used the epithelial cell adhesion molecule (EpCAM) as a target for enriching tumor-derived EVs.[23,38-41] Other disease-specific markers have also been used to isolate subpopulations of EVs that are more related to the disease.[27,28]

Different types of mRNA analysis techniques have been reported in the context of EVs, but only a few studies have utilized the NanoString nCounter assay for liquid biopsy markers.[19,38,42-44] Our study reported herein utilized a novel approach for exo-mRNA analysis, which included a microfluidic EV affinity purification (EV-MAP) chip that enriched two orthogonal tumor-derived EV subpopulations: (i) EVs sourced from epithelial cells and (ii) EVs collected from cells with a mesenchymal phenotype. The exo-mRNA from both subpopulations were subjected to the nCounter PAM50/Prosigna assay without requiring amplification to identify breast cancer (BC) molecular subtypes: luminal A, luminal B, basal-like, and HER2-enriched. We have reported a dualaffinity selection strategy using anti-EpCAM and anti-FAPα (fibroblast activation protien α) mAbs, but it was used to isolate circulating tumor cells.[45]

EVs expressing EpCAM (EV^{EpCAM}) and FAPα ($EV^{FAP\alpha}$)[45] were isolated using an EV-MAP microfluidic device. The purified EVs were then used for exo-mRNA transcript analysis via RT-ddPCR and PAM50 gene profiling (50 test genes and 8 reference genes) via the Nanostring nCounter to determine exo-mRNA abundance associated with a particular molecular subtype of BC for prognostication and risk-of-recurrence assessment. As such, the

PAM50 assay is not used to diagnose BC in patients, but instead molecular sub-type patients already diagnosed with BC to allow for assignment of proper treatment (i.e, prognostic test). Formalin-fixed paraffin-embedded (FFPE) tumor tissue was profiled as well to serve as the "gold standard" for determining the accuracy of using exo-mRNA for discerning the molecular subtype.

MATERIALS AND METHODS

Reagents and Materials.

Please see the Supporting Information for details on all reagents used in this study.

Cell Culture and EV Harvesting.

Please see the Supporting Information for details on cell lines and culturing conditions.

EV-MAP Device Fabrication.

EV-MAP devices, which were similar in design to our previous reports,[46] used in this study were provided by BioFluidica and fabricated in the cyclic olefin polymer (COP, ZEONOR 1020/1060) via injection molding (Stratec, Austria) from a mold insert made via UV-LiGA.[47] The device's surfaces were activated with UV/O_3 for generation of surface COOH functionalities for the covalent attachment of affinity agents.[48]

Antibody Immobilization.

Monoclonal antibody (mAb) immobilization to the surface of the EV-MAP chip followed procedures from our previous publications (see the Supporting Information for details).[45,46,49]

Sample Preparation and Automated Sample Processing Using EV-MAP.

Please see the Supporting Information for more details.

EV Lysis for Total RNA Extraction.

Please see the Supporting Information for experimental details.

Reverse Transcription.

Please see the Supporting Information for further details.

Droplet Digital PCR.

Please see the Supporting Information for details on the equipment and procedures for ddPCR.

PAM50 Gene Signature Assay.

Please see the Supporting Information for experimental details.

EV Release.

For the affinity-selected EVs' evaluation using nanoparticle tracking analysis (NTA) and transmission electron microscope (TEM), particles were released from the isolation chip by infusing 0.2% proteinase K in PBS buffer (pH 7.4) and incubated at 37 °C for 30 min. Released EVs were eluted with PBS (10 μL/min, 7 min).

Nanoparticle Tracking Analysis and TEM for EV Characterization.

Please see the Supporting Information.

Monte Carlo Fluid Dynamics Simulation of EV-MAP.

Experimental details, simulation parameters, and modeling are provided in the Supporting Information.

RESULTS AND DISCUSSION

EV-MAP Microfluidic Design, Optimization, and Fabrication.

The EV-MAP was fabricated in the cyclic olefin polymer, COP, via injection molding (Figure 1a,b). The microfluidic network was composed of 7 parallel selection beds (30 mm long and 4 mm wide) filled with diamond-shaped micropillars (10 × 10 μm) with the beds addressed using a single inlet and outlet channel (200 × 200 μm) arranged in the so-called *z*-configuration. The table in Figure 1c summarizes the dimensional features of this chip.

The challenge with some microfluidics is their production, which cannot support generation of a large number of devices with tight compliancy to support in vitro diagnostics. For example, a vast number of EV isolation platforms are fabricated in polydimethylsiloxane (PDMS), which is not conducive to high-scale manufacturing required for large-scale studies. Wijerathne et al.[46] and Reátegui et al.[16] reported microfluidics for EV isolation that used a thermoplastic chip fabricated via injection molding; the chip used herein was produced via injection molding.

As the sample is hydrodynamically shuttled through the EV-MAP chip, EVs move laterally around the pillars and encounter surface-bound mAbs under laminar flow conditions. A small inter-pillar spacing decreases diffusional distances to increase the number of interactions between surface-immobilized mAbs and the EVs, which improves recovery. To gauge the efficiency of the EV-MAP for recovering solution-borne EVs using a surface-bound mAb, a Monte Carlo simulation was used considering EV diffusion and EV-mAb binding kinetics. While COMSOL can simulate these physics, accurate estimation of EV recovery required modeling diffusion through the entire EV-MAP bed, which became numerically intractable, given the large geometry of each bed. The Monte Carlo simulation tracked the diffusive and convective motions of individual EVs through an EV-MAP bed (see the Supporting Information)[50] and simulated the probability of mAb–EV binding based on the Chang–Hammer model.[51] Binding kinetics between the solution-borne EV and surface-bound mAbs were important to evaluate as not every interaction with a surface results in successful association of an EV to the surface-mAb due to orientational effects.

Simulation results can be found in the Supporting Information (Figure S1 and simulation parameters provided in Table S2). When an EV encountered a surface-attached mAb, EV–mAb binding kinetics were invoked to result in either a successful binding event or continued motion of the EV through a pillared bed (Figure S1). The results were averaged over thousands of EV events until the simulation converged to provide an average EV-MAP recovery (Figure 1d). Due to the low Peclet number near the channel surface created by the no-slip condition, the motion of an EV was primarily diffusion-controlled near the pillar's surface. As expected, we found that decreasing the inter-pillar spacing or increasing the bed length increased recovery. For the EV-MAP device, a volume flow of 13 μL/min provided recoveries of ~80%, but even at a volume flow of 20 μL/min, the recovery was still ~60% (Figure 1d). We also generated shear stress profiles from COMSOL Multiphysics simulations using parameters listed in Table S2. The shear stress and laminar flow simulation results are shown in Figure 1e. Results showed a shear stress of 3.1 dynes/cm^2 at the pillar wall for a linear velocity of 3.7 mm/s. Due to the small size of EVs and high strength of the mAb–antigen association as well as the covalent attachment of the mAb to the microfluidic surface, fluid shear forces could not remove EVs from the surface.[49] A single mAb–antigen bond (1.2×10^{-5} dynes)[52] indicated that a 100 nm EV would require 150,000 dynes/cm^2 for physical removal from the surface.

We estimated a particle load of ~2.2×10^{11} (Figure 1c), which was determined by the surface density of mAbs, its orientation on the surface following EDC/NHS coupling chemistry, and the total surface area of the device (38 cm^2). The surface density of −COOH groups following UV/O_3 activation of thermoplastics is 3.7×10^{-4} molecules nm^{-2},[53] which would generate an mAb load per device of 1.4×10^{12}. However, because of the stochastic nature of the attachment of mAbs to the surface, which depends on the availability of a primary amine group resident on the mAb, nearly 90% of the mAbs may be shielded by the surface following immobilization, resulting in 1.4×10^{11} available sites.[46] The high surface load, which was enabled by the placement of 7 beds with each bed populated with a high density of pillars, provided a high mass load and large dynamic range, which is necessary to generate quantitative data with respect to the expression of exo-mRNA targets.

Wei et al. reported that a single EV can carry ~4.45 ng of total RNA, which would indicate ~445 ng of total RNA from ~10^{11} particles at chip saturation. As can be seen from Table S5, we never exceeded the calculated saturation point as indicated by a total RNA yield of 445 pg per chip isolate. The total RNA mass for all samples analyzed ranged between 0.4 and 50 ng.

Automated Fluidic Operation of the EV-MAP Chip.

EV-MAP chips were operated using the LiquidScan (Bio-Fluidica, Inc.; Figure 1f) liquid handling robot. The Liquid-Scan operation of the EV-MAP chip increased our sample processing throughput (the robot has 16 pipetting channels and can process 8 chips simultaneously) and reduced intersample variability compared to manual chip operation using a syringe pump. The interface between the robot and the EV-MAP chip adopted a format shown in Figure 1g,h; the EV-MAP's input/output ports interfaced directly to the robot using a pipet tip.

The work deck of the liquid handling robot was modified to accommodate the fluidic operation of the chips by using a push/pull operational mode. The robot could simultaneously operate 8 chips and required approximately 80 min per assay (500 μL input plasma volume and 1 mL wash), meaning that 144 EV isolation assays could be run per machine per day and do so in a fully automated fashion. Manual operation of the EV-MAP chip, which required attended operation, using a multi-channel syringe pump allowed only ~32 assays per day.

Chip Preparation, Protocol Optimization, and EV Characterization.

EV purification utilized anti-EpCAM and anti-FAPα mAbs with each EV-MAP chip containing a single mAb type (Figure 2a). mAbs were covalently attached to the EV-MAP chip surface following UV/O_3 activation of the chip, which created surface carboxylic acids.[53] The mAbs were attached to the surface −COOH groups using standard EDC/NHS coupling chemistry (Figure 2b). COP has demonstrated the ability to efficiently produce carboxylic acid surfaces following UV/O_3 activation.[46,53] This property makes this material attractive for the EV-MAP chip because high −COOH surface densities result in high mAb loads that increase the recovery and load of selected targets.[48] Throughout this study, we confirmed successful EDC/NHS coupling of the mAbs to the chip surface using 5′-NH_2, 3′-Cy3 oligonucleotide fluorescent reporters (Figure S2).

To minimize non-specific adsorption, various blocking and washing buffers were evaluated. The level of non-specific adsorption was measured by processing 500 μL of four different plasma samples using anti-EpCAM, anti-FAPα, anti-CD81, and anti-$IgG2_A$ (negative control) mAb-modified devices. EVs were released from the device's surfaces, and nanoparticle concentrations were measured using NTA (size distribution results are shown in Figure S3). We measured the specificity, which was calculated by subtracting the EV counts released from the isotype device (i.e., non-specifically adsorbed particles) from the anti-EpCAM device particle number and dividing by the total number of EVs found in the eluent of the device. Specificity was also assessed using ddPCR performed on exosomal total RNA.

Different blocking and washing buffers were evaluated: (i) 1% BSA; (ii) 1% BSA/1% PVP-40/Tween 20 in TBST; and (iii) 1% BSA/1% PVP-40. Devices were pre-washed with 1 mL of blocking buffer at 50 μL/min. After EV isolation, devices were washed with 1 mL of the appropriate buffer at 25 μL/min. Following sample processing, EVs were either released intact or exosomal total RNA was harvested from the on-chip lysis of EVs.

Blocking and washing EV-MAP surfaces with 1% BSA in PBS resulted in the lowest specificity from NTA (16%) using the anti-EpCAM device. Specificity was calculated by subtracting the nonspecific $IgG2_B$ EV nanoparticle concentrations from the anti-EpCAM EV concentrations and dividing by the total number of nanoparticles collected as measured by NTA (see Figures 2c and S3). Further NTA data indicated that the addition of 1% PVP-40 to the BSA blocking buffer while washing devices with 0.2% Tween-20 achieved the highest specificity, which was found to be 42% (Figure 2c). We also assessed EV-MAP specificity through exo-mRNA quantification, and this resulted in a specificity of 99 ± 1% using a blocking buffer of 1% BSA/1% PVP-40 and was washed with 0.2% Tween-20 (Figure 2c).

We also assessed EV-MAP purification of cell-specific EV subpopulations and their exo-mRNA expression. 500 μL of healthy donor plasma was infused into two sets of devices functionalized with anti-EpCAM, anti-FAPα, anti-CD81, or anti-IgG_{2B} mAbs. Devices were blocked with 1% BSA/1% PVP-40 and washed with 0.2% Tween 20. After washing, one set of devices was treated with proteinase K for release of EVs to allow for TEM (Figure 2d), while another set was subjected to on-chip lysis and RNA solid-phase extraction (Figure 2e) followed by RT-ddPCR (Figure 2f).

TEM images of the EV-MAP eluent showed the presence of EVs through observation of a cup-shaped morphology, which is characteristic of EVs. Although nanoparticles were present in the isotype negative control fraction, most of those particles were very small with diameters <20 nm, but not resembling aggregated proteins (Figure 2d). The presence of EVs in the mAb isolated fractions, including very small particles in the IgG_{2B} isotype negative control, was verified by extraction of total RNA and subjecting each extract to TapeStation analysis (Figure 2e). Total RNA was extracted from affinity-isolated EV^{EpCAM}, $EV^{FAP\alpha}$, and EV^{CD81}, and total RNA was also recovered from the IgG_{2B} isotype negative control. However, very little expression of the genes tested was found in the fraction isolated on the isotype chip, but discernible amounts of exo-mRNA from the anti-EpCAM, anti-FAPα, and anti-CD81 chips were observed. Transcript expression between certain genes including epithelial (*EpCAM* and *CK19*), mesenchymal (*FAPα* and *VIM*), cytokine (*IL8*), tetraspanin (*CD81*), and stem-cell related (*CD24* and *CD44*) genes was evaluated using ddPCR (Figure 2f). Total RNA traces indicated that the RNA sizes ranged from 50 to 500 nt, which represents typical exosomal total RNA sizes.[15]

The isolation of EV^{EpCAM} and $EV^{FAP\alpha}$ from healthy donor plasma resulted in the appearance of epithelial- and mesenchymal-associated gene transcripts. We found high expression of *CK19* and low expression of the mesenchymal-associated *FAPv2* and *VIM* in the anti-EpCAM isolate but low expression of *CK19* and high expression of *FAPv2* and *VIM* for the anti-FAPα isolate (Figure 2f). *CD44*(high)/*CD24*(low) occurred in the anti-FAPα fraction, correlating well with the mesenchymal phenotype.

Figure 2g shows fluorescence images of an EV-MAP with no mAb attached to the surface and a positive control (anti-EpCAM mAb covalently attached to the chip surface) collected from SKBR3 cell line medium processed using the EV-MAP chip and stained with anti-EpCAM–Cy5 mAbs. Following affinity isolation and staining, the material within the device was lysed and the fluorescence signal was collected for both negative and positive (anti-EpCAM-modified chip) controls. There was a difference in the fluorescence intensity between these two controls, indicating successful affinity selection of EV^{EpCAM} particles.

Orthogonality of Selection Markers.

Orthogonality of selection markers would result in gene expression profiles and the proteins they express not being co-expressed to any substantial degree in different cell types. Non-orthogonal selection markers would indicate that the dual selection process would not offer unique or complementary molecular information. To investigate whether EV^{EpCAM} and $EV^{FAP\alpha}$ were orthogonal, conditioned cell culture media collected from two BC cell lines with epithelial and mesenchymal phenotypes were processed using the

EV-MAP. The SKBR3 cell line represents an epithelial phenotype—EpCAM(+)/FAPα(−), and Hs578T has a mesenchymal-like phenotype [EpCAM(−)/FAPα(+)], as shown in Figure 3a.[45] Immunophenotyping of the SKBR3 and Hs578T (Figure 3a) cells showed the typical pattern indicative of epithelial and mesenchymal cells, respectively. For example, SKBR3 cells showed high expression of *EpCAM* but no noticeable expression of *FAPα*, while no *EpCAM* expression was seen in the Hs578T cells, but high expression of *FAPα* was observed.

For EV purification, cell culture media was EV-depleted (further information provided in Figures S4 and S5) to eliminate background bovine EVs. EV depletion created little differences in the gene expression profiles when compared to cells grown in regular FBS (Figure S6). 500 μL of conditioned culture media was processed through either an anti-EpCAM, anti-FAPα, or anti-IgG_{2A} isotype control EV-MAP chip. The isotype was used to assess the level of non-specific binding.[34,36,54] To release EVs for NTA and TEM analysis, we employed 0.2% proteinase K in PBS for 30 min at 37 °C. Intact EVs were observed following release (Figure S7a-c), and the release efficiency was found to be 99 ± 1% (Figure S6c).

TEMs of the EV^{EpCAM} and $EV^{FAP\alpha}$ from SKBR3 and Hs578T culture media, respectively, showed no differences in the size of the EVs and were comparable in size and morphology to the EVs isolated via ultracentrifugation (Figure 3b,c). NTA results showed that the size of EV-MAP-purified EVs ranged from 30 to 300 nm with an average size of ~125 nm. NTA results for SKBR3 EVs showed more than twice the number of nanoparticles selected by the anti-EpCAM device (Figure 3b) compared to the FAPα device from the same volume of medium.

Through TEM analysis, some EVs were observed to have the “cup-shape” morphology typically seen in EVs, but the majority were spherical in shape (Figure 3b). No particles were present in the TEM images from the isotype fractions. This suggested that particles detected for the isotype control were from the background associated with the NTA method and confirms the previously reported lack of specificity for particle enumeration via NTA.[55-57]

Conditioned media was processed via the EV-MAP with anti-EpCAM and anti-FAPα mAb chips with subsequent total RNA extraction followed by RT–ddPCR. Cells were also taken from conditioned cell media and subjected to lysis, RNA extraction, and RT–ddPCR. Primers for ddPCR were designed to span the sequence of mRNA close to the 3′ poly adenylated region with the interrogated regions ranging from 240 to 470 nt. The gene expression profiles were then compared between the selected EVs and their cells-of-origin to determine whether EVs could provide similar information to that from their cells-of-origin. The gene panel we analyzed (Figure 3d) contained epithelial (*EpCAM*, *CRT*, and *CD24*) and mesenchymal (*FAPα*, *CD44*, *SMA*, and *VIM*) genes as well as a cytokine gene (*IL8*). The gene expression patterns agreed fairly well with the expression pattern of the cells with no expression of FAPα seen in the SKBR3 cells but high expression in the Hs578T cells. Also, no mesenchymal mRNA transcripts were detectable in the SKBR3 cells, but they were present in the Hs578T cells. The SKBR3 and Hs578T cell lines are distinguishable

not only based on their expression of epithelial and mesenchymal markers but also by their *CD44/CD24* expression ratio as Hs578T cells were *CD44*(high)/*CD24*(low), while SKBR3 cells were *CD44*(low)/*CD24*(high).[58]

The same epithelial/mesenchymal panel was used to evaluate mRNA abundance in EVs isolated from healthy donors and 3 BC patients' plasma. Blood samples from healthy donors were secured from women arriving for routine mammograms and known to have no current diagnosis of cancer (further healthy donor and patient information can be found in Table S3 and S4).

To compare healthy donors and BC patients' gene expression profiles resulting from the EVs purified via the EV-MAP chip, 500 μL of plasma was processed using anti-EpCAM and then anti-FAPα chips with the optimized blocking and washing buffers. After processing, EVs were lysed on-chip for RNA purification and then subjected to RT–ddPCR Results from RT–ddPCR are presented in Figure 3e. The abundance of mRNA transcripts in both EV^{EpCAM} and $EV^{FAP\alpha}$ for the genes evaluated showed higher levels of the transcripts in BC patients compared to healthy donors. Following principal component analysis (PCA) of the mRNA transcripts, a gene cluster for healthy donors was observed, while the data for BC EVs were outside of this cluster. Only one BC sample fell within the healthy donor cluster (Figure 3f). Copy numbers for cDNA (i.e., mRNA) were low but above the levels of the negative controls and above the limit of detection of ddPCR (empirically determined in our hands to be 4 copies).[59]

Proof-of-Concept Study for Molecular Subtyping BC Patients' Using mRNA Sourced from EV^{EpCAM} and $EV^{FAP\alpha}$.

EV mRNA analysis of cancer patients is not trivial because of the low mass of exo-mRNA.[13] Owing to the efficient recoveries and high specificity of the EV-MAP device, we secured sufficient total RNA to directly analyze exo-mRNAs using the PAM50 genes. The Prosigna assay uses the PAM50 mRNA gene panel and an established algorithm[30] to classify BC patients using the NanoString nCounter Dx instrument. Because the Prosigna assay is not used for diagnostic purposes, the EVs and exo-mRNA from healthy donors' plasma were not included in the analysis in this work. The four intrinsic subtypes of BC, i.e., luminal A, luminal B, HER2-enriched, and basal-like, are defined by differential expression of 50 test genes and 8 reference genes.

For these studies, we evaluated the PAM50 gene panel expression using the nCounter with BC patients' samples. The assay is designed to use FFPE tumor tissue. Evaluation of the concentration of the total RNA isolated from EV^{EpCAM}, $EV^{FAP\alpha}$, and EV^{CD81} is shown in Figure 4a. Total RNA concentration was the highest in the EV^{CD81} population and proportional to the highest number of particles isolated on the CD81 EV-MAP chip. Total RNA isolated from EV^{EpCAM} or $EV^{FAP\alpha}$ was not significantly different in all subtypes of BC. Total RNA concentration from healthy donors and all subtypes of BC was not statistically different as well. From 0.5 mL of healthy donor plasma, EV^{EpCAM} and $EV^{FAP\alpha}$ provided 0.8 ± 0.5 ng (range 0.05–1.6 ng) and 1.25 ± 1.0 ng (range 0.05–2.75 ng) of total RNA, respectively. The total RNA mass from EV^{EpCAM} and $EV^{FAP\alpha}$ from 0.5 mL of BC patient's plasma was 2.25 ± 2 ng (range 0.05–11.1 ng) and 2.25 ± 4 ng (range 0.05–24.4 ng),

respectively. The total RNA mass extracted from EV^{CD81} averaged 8.0 ± 9 ng (range 0.8–25.5 ng) and was statistically different from total RNA found in $EV^{FAP\alpha}$ but not EV^{EpCAM}. Total RNA electrophoretic profiles varied between samples for all three subpopulations of EVs. Representative electropherograms are shown in Figure S8 for EV^{EpCAM}, $EV^{FAP\alpha}$, and EV^{CD81}. The fragment sizes of total RNA ranged between 30 and 1000 nt, and in some samples, evidence of fragmented rRNA was seen (note the short length of 18S and 28S rRNA, which typically possess a size of 2 and 5 kb, respectively).

Further analysis of total RNA for different subtypes of BC (identified based on tumor tissue analysis) is shown in Figure 4b, which showed that total RNA concentration was the highest in the basal molecular subtype for both EV^{EpCAM} and $EV^{FAP\alpha}$. In luminal A, total RNA was highest in the EV^{EpCAM} subpopulation. HER-2 and luminal B subtypes showed the lowest concentration of total RNA for both EV^{EpCAM} and $EV^{FAP\alpha}$. Total RNAs from EV^{EpCAM} and EV^{FAPa} introduced into the PAM50 assay are listed in Table S5. Inspection of the heatmap shown in Figure 4c clearly indicates that the amount of mRNA needed for the PMA50 genes was much higher than what we could garner from the EVs irrespective of the subpopulation.

PCA of all exo-mRNA transcripts (Figure 4d) for the PAM50 panel showed different clusters for EVs and tumor tissue; however, poor classification efficiency between BC subtypes was observed. Analysis of transcript abundance showed high correlation in mRNA transcript abundance between EV^{CD81} and $EV^{FAP\alpha}$ or EV^{EpCAM} (75–102%, as deduced from the slopes of the curves) but very low correlation of all three with tumor tissue mRNA (0.5–14.4%; Table S6). Even mRNA profiles for EVs isolated via PEG precipitation and tumor tissue showed low concordance (8–32%), meaning that only ~32% of the same transcripts were present in both fractions.

We could identify different clusters that were clearly present in the tumor tissue and different ones in the exo-mRNA. The black box in Figure S9a marks the FFPE clusters, while blue and green boxes represent the more abundant and less abundant transcripts in FFPE vs EVs, respectively. For example, the genes *GRB7, ERBB2, MYC, KRT14, MMP11, GPR160, CXXC5, SLC39A6*, and *MDM2* were highly abundant in FFPE tissue but not detected in the EVs. Furthermore, transcripts for genes such as *CDC6, CENPF, CEP55, EXO1, MELK, UBE2C, ACTR3B, SFRP1, MLPH, FOXA1, BLVRA*, and *BAG1* showed higher abundance in EVs compared to FFPE (see Table S7).

Overall, 36 of the 50 genes used in the PAM50 panel had no detectable expression in >40% of the samples. Therefore, for exo-mRNA, ~14 genes of the original PAM50 panel were used for the molecular subtyping. We also investigated whether the transcript length influenced the PAM50 subtyping results. Figure S9b shows the genes in the PAM50 panel and their corresponding length. We concluded that the gene length did not cause bias.

Based on these results, we generated an exo-mRNA expression profile for the samples evaluated in this study, including the FFPE tissue using the nCounter assay for unamplified mRNA. A heatmap is shown in Figure 4e (log2 profile) for a set 14 genes that withstood our filtering procedure and were used to hierarchically cluster all EV subpopulations and

FFPE samples. The nCounter assay uses 8 genes as housekeeping genes for normalization. As can be seen from Figure 4f, for these 8 housekeeping genes, we selected to use PUM1 as the normalization gene because it provided minimal changes in its exo-mRNA expression across the EV subpopulations investigated (EV^{EpCAM}, $EV^{FAP\alpha}$, EV^{TOT}, and EV^{CD81}). The heatmap in Figure 4e shows that the FFPE samples were fairly well clustered, consistent with the PCA analysis shown in Figure 4d, indicating differences in the abundance of mRNA transcripts packaged into EVs compared to their cell-of-origin (see Figure S9a). However, the molecular subtype clustering was not evident in the exo-mRNA heatmap consistent with our PCA analysis (see Figure 4d).

Computational Algorithm for Breast Cancer Molecular Subtyping Using exo-mRNA.

Our initial analysis of the relative levels of the PAM50 genes using an algorithm developed previously[30] did not successfully classify BC molecular subtypes from exo-mRNA. Using four different EV subpopulations (i.e., total EVs, EV^{EpCAM}, $EV^{FAP\alpha}$, and EV^{CD81}), only 1 of 8 samples was successfully called using exo-mRNA sourced from EV^{EpCAM} and $EV^{FAP\alpha}$ and 0 out of 8 using total EVs or EV^{CD81}. Therefore, we decided to modify our approach, and instead of using all 50 genes, we sought to use subsets of the 50-gene panel and develop a new algorithm (exo-PAM50) to classify the molecular subtypes (see the Supporting Information for more information on development of this algorithm and Figure S10 for a flowchart of processing steps and Tables S8-S11 for the associated Supporting Information).

Across the various EV subpopulations, between 12 and 15 genes withstood filtering and were subjected to the exo-PAM50 algorithm that identified 4 unique gene sets, resulting in 75% concordance between the molecular subtyping calls made from EV^{EpCAM} and those obtained from FFPE tumor tissue. For $EV^{FAP\alpha}$, 5 subsets were identified, of which 3 resulted in 75% concordance between the molecular subtyping calls made from $EV^{FAP\alpha}$ and those obtained from FFPE tumor tissue. For EV^{CD81}, only 1 gene subset was identified that led to 75% concordance, and for total EVs isolated by ExoRNeasy, 2 gene subsets led to 63% concordance with the molecular subtyping calls from FFPE tumor tissue. All subsets of genes were unique within and between EV sample types. Gene sets that correctly predicted the subtype based on exo-mRNA in EV^{EpCAM} did not perform well for predicting the subtype in $EV^{FAP\alpha}$.

Figure 4g presents PAM50 gene profiling results for specific BC molecular subtypes. $EV^{FAP\alpha}$ could not correctly identify the basal BC subtype, while EV^{EpCAM} identified this molecular type correctly for all gene panels. However, the $EV^{FAP\alpha}$ subpopulation identified luminal A, luminal B, and HER-2 subtypes with 100% accuracy using gene panels 5, 6, 7, and 9. Analysis of the EV^{EpCAM} and $EV^{FAP\alpha}$ data revealed that a successful calling protocol could be established: (i) consensus of the majority of gene panels for both EV^{EpCAM} and $EV^{FAP\alpha}$ dictates the molecular subtype and (ii) when the EV^{EpCAM} subpopulation called the basal subtype, those data were used for the molecular subtype classification. Luminal A and luminal B calls were made solely by the $EV^{FAP\alpha}$ data, and the HER-2 subtype could use both the EV^{EpCAM} and $EV^{FAP\alpha}$ subpopulation results. Using this strategy, 100% call accuracy was achieved using unamplified exo-mRNA sourced from EV^{EpCAM} and $EV^{FAP\alpha}$.

However, when using EV^{CD81} or ultracentrifuge isolated EVs, the BC subtype identification accuracy was 75%, irrespective of the gene subset(s) used.

CONCLUSIONS

FDA-approved tests such as the Oncotype DX or the Prosigna BC prognostic gene signature assay analyze mRNA extracted from a solid BC tissue to indicate survival based on expression of selected genes,[30] which requires an invasive procedure to secure the test sample and subsequent formalin fixation and paraffin embedment that can degrade the integrity of the RNA. The ability to translate our dual-selection EV-MAP procedure into current clinical applications using a liquid biopsy sample, which provides minimally invasive sampling, was demonstrated for the molecular subtyping of BCs. However, slight modifications in the tissue-based assay were required such as the genes used in the analysis; an exo-PAM50 test panel was developed that took advantage of the dual isolation approach adopted herein. The challenge with many molecular assays for a clinical indication is that they require large mass inputs; for example, the Prosigna test requires >12.5 ng/μL of total RNA, which in many cases a liquid biopsy sample cannot provide. Our dual-selection EV-MAP assay addressed this concern by implementing special design considerations including a number of parallel beds (7), high recovery, and high purity with the selection of both epithelial- and mesenchymal-like EVs. In addition, we developed a new algorithm (exo-PAM50), which did not include genes that were “silent” in exo-mRNA (i.e., genes were removed if samples contained >40% zero values for a particular transcript).

Given the success of these studies, which were a proof-of-concept clinical study, our future work will evaluate larger gene panels and expand on including low abundant or “silent” genes, which can be informative when predicting the BC subtype as well. We will also seek to perform a powered clinical study to further substantiate our findings associated with using exo-mRNA for molecular subtyping BC patients. In addition, we will evaluate EVs isolated from other epithelial cancers using EpCAM and FAPα targets[45] and the use of different molecular assays from EVs enriched using our EV-MAP device, such as RNA-Seq. While early-stage disease would be expected to produce less EVs and consequently a lower mRNA mass, it will be necessary to consider alternative mRNA expression platforms that will provide lower limits of detection.

Supplementary Material

Refer to Web version on PubMed Central for supplementary material.

ACKNOWLEDGMENTS

We are grateful to patients for their generous donations of tissue and blood samples. This work was supported in part by an NIH Small Business Innovation Research (SBIR) (R43CA232848-01) award. The authors also thank the NIH for financial support of this work through the Biotechnology Resource Center of BioModular Multi-scale Systems for Precision Medicine (P41-EB020594) and the Kansas Institute for Precision Medicine (P20-GM130423). The authors also acknowledge the KU Nanofabrication Facility (KUNF; P20-GM103638) and the staff of the KUMC/KUCC Biospecimen Repository Core Facility (P30-CA168524) including Lauren DiMartino, Michele Park, and Alex Webster for helping obtain human specimens, the KUMC Biomarker Discovery Laboratory, and the KU Microscopy and Analytical Imaging Laboratory.

REFERENCES

(1). Yáñez-Mó M; Siljander PRM; Andreu Z; Bedina Zavec A; Borràs FE; Buzas EI; Buzas K; Casal E; Cappello F; Carvalho J; et al. J. Extracell. Vesicles 2015, 4, 27066. [PubMed: 25979354]

(2). Veziroglu EM; Mias GI Front. Genet 2020, 11, 700. [PubMed: 32765582]

(3). Trinidad CV; Tetlow AL; Bantis LE; Godwin AK Cancer Prev. Res 2020, 13, 241–252.

(4). Jeppesen DK; Fenix AM; Franklin JL; Higginbotham JN; Zhang Q; Zimmerman LJ; Liebler DC; Ping J; Liu Q; Evans R; et al. Cell 2019, 177, 428–445. [PubMed: 30951670]

(5). O'Grady T; Njock M-S; Lion M; Bruyr J; Mariavelle E; Galvan B; Boeckx A; Struman I; Dequiedt F BMC Biol. 2022, 20, 72. [PubMed: 35331218]

(6). Li Y; He X; Li Q; Lai H; Zhang H; Hu Z; Li Y; Huang S Comput. Struct. Biotechnol. J 2020, 18, 2851–2859. [PubMed: 33133426]

(7). Fiskaa T; Knutsen E; Nikolaisen MA; Jørgensen TE; Johansen SD; Perander M; Seternes OM PLoS One 2016, 11, No. e0161824. [PubMed: 27579604]

(8). Fischer S; Deind E Appl. Sci 2021, 11, 7250.

(9). Vlassov AV; Magdaleno S; Setterquist R; Conrad R Biochim. Biophys. Acta, Gen. Subj 2012, 1820, 940–948.

(10). Valadi H; Ekström K; Bossios A; Sjöstrand M; Lee JJ; Lötvall JO Nat. Cell Biol 2007, 9, 654–659. [PubMed: 17486113]

(11). Skog J; Würdinger T; van Rijn S; Meijer DH; Gainche L; Curry WT Jr.; Carter BS; Krichevsky AM; Breakefield XO Nat. Cell Biol 2008, 10, 1470–1476. [PubMed: 19011622]

(12). Crescitelli R; Lässer C; Szabó TG; Kittel A; Eldh M; Dianzani I; Buzás EI; Lötvall J J. Extracell. Vesicles 2013, 2, 20677.

(13). Wei Z; Batagov AO; Schinelli S; Wang J; Wang Y; El Fatimy R; Rabinovsky R; Balaj L; Chen CC; Hochberg F; et al. Nat. Commun 2017, 8, 1145. [PubMed: 29074968]

(14). Jenjaroenpun P; Kremenska Y; Nair VM; Kremenskoy M; Joseph B; Kurochkin IV PeerJ 2013, 1, No. e201. [PubMed: 24255815]

(15). van Niel G; D'Angelo G; Raposo G Nat. Rev. Mol. Cell Biol 2018, 19, 213–228. [PubMed: 29339798]

(16). Reátegui E; van der Vos KE; Lai CP; Zeinali M; Atai NA; Aldikacti B; Floyd FP; Khankhel HA; Thapar V; Hochberg FH; et al. Nat. Commun 2018, 9, 175. [PubMed: 29330365]

(17). Keup C; Mach P; Aktas B; Tewes M; Kolberg H-C; Hauch S; Sprenger-Haussels M; Kimmig R; Kasimir-Bauer S Clin. Chem 2018, 64, 1054–1062. [PubMed: 29769179]

(18). Chen WW; Balaj L; Liau LM; Samuels ML; Kotsopoulos SK; Maguire CA; LoGuidice L; Soto H; Garrett M; Zhu LD; et al. Mol. Ther.–Nucleic Acids 2013, 2, No. e109. [PubMed: 23881452]

(19). Bracht JWP; Gimenez-Capitan A; Huang C-Y; Potie N; Pedraz-Valdunciel C; Warren S; Rosell R; Molina-Vila MA Sci. Rep 2021, 11, 3712. [PubMed: 33580122]

(20). Xu H; Dong X; Chen Y; Wang X Clin. Chem. Lab. Med 2018, 56, 479–484. [PubMed: 29252188]

(21). Goldvaser H; Gutkin A; Beery E; Edel Y; Nordenberg J; Wolach O; Rabizadeh E; Uziel O; Lahav M Br. J. Cancer 2017, 117, 353–357. [PubMed: 28641311]

(22). Royo F; Zuñiga-Garcia P; Sanchez-Mosquera P; Egia A; Perez A; Loizaga A; Arceo R; Lacasa I; Rabade A; Arrieta E; et al. J. Extracell. Vesicles 2016, 5, 29497. [PubMed: 26895490]

(23). Dong J; Zhang RY; Sun N; Smalley M; Wu Z; Zhou A; Chou S-J; Jan YJ; Yang P; Bao L; et al. ACS Appl. Mater. Interfaces 2019, 11, 13973–13983. [PubMed: 30892008]

(24). Davey M; Benzina S; Savoie M; Breault G; Ghosh A; Ouellette R Int. J. Mol. Sci 2020, 21, 8330. [PubMed: 33172003]

(25). Vitale SR; Helmijr JA; Gerritsen M; Coban H; van Dessel LF; Beije N; van der Vlugt-Daane M; Vigneri P; Sieuwerts AM; Dits N; et al. BMC Cancer 2021, 21, 315. [PubMed: 33761899]

(26). Sun N; Tran BV; Peng Z; Wang J; Zhang C; Yang P; Zhang TX; Widjaja J; Zhang RY; Xia W; et al. Adv. Sci 2022, 9, 2105853.

(27). Sun N; Lee Y-T; Zhang RY; Kao R; Teng P-C; Yang Y; Yang P; Wang JJ; Smalley M; Chen P-J; et al. Nat. Commun 2020, 11, 4489. [PubMed: 32895384]

(28). Wang JJ; Sun N; Lee Y-T; Kim M; Vagner T; Rohena-Rivera K; Wang Z; Chen Z; Zhang RY; Lee J; et al. Nano Today 2023, 48, 101746. [PubMed: 36711067]

(29). Perou CM; Sørlie T; Eisen MB; van de Rijn M; Jeffrey SS; Rees CA; Pollack JR; Ross DT; Johnsen H; Akslen LA; et al. Nature 2000, 406, 747–752. [PubMed: 10963602]

(30). Parker JS; Mullins M; Cheang MCU; Leung S; Voduc D; Vickery T; Davies S; Fauron C; He X; Hu Z; et al. J. Clin. Oncol 2009, 27, 1160–1167. [PubMed: 19204204]

(31). Contreras-Naranjo JC; Wu H-J; Ugaz VM Lab Chip 2017, 17, 3558–3577. [PubMed: 28832692]

(32). Shirejini SZ; Inci F Biotechnol. Adv 2022, 54, 107814. [PubMed: 34389465]

(33). Chen J; Li P; Zhang T; Xu Z; Huang X; Wang R; Du L Front. Bioeng. Biotechnol 2022, 9, 811971. [PubMed: 35071216]

(34). Chen C; Skog J; Hsu C-H; Lessard RT; Balaj L; Wurdinger T; Carter BS; Breakefield XO; Toner M; Irimia D Lab Chip 2010, 10, 505–511. [PubMed: 20126692]

(35). Kanwar SS; Dunlay CJ; Simeone DM; Nagrath S Lab Chip 2014, 14, 1891–1900. [PubMed: 24722878]

(36). Ashcroft BA; de Sonneville J; Yuana Y; Osanto S; Bertina R; Kuil ME; Oosterkamp TH Biomed. Microdevices 2012, 14, 641–649. [PubMed: 22391880]

(37). Yoshioka Y; Kosaka N; Konishi Y; Ohta H; Okamoto H; Sonoda H; Nonaka R; Yamamoto H; Ishii H; Mori M; et al. Nat. Commun 2014, 5, 3591. [PubMed: 24710016]

(38). Kamyabi N; Abbasgholizadeh R; Maitra A; Ardekani A; Biswal SL; Grande-Allen KJ Biomed. Microdevices 2020, 22, 23. [PubMed: 32162067]

(39). Fang S; Tian H; Li X; Jin D; Li X; Kong J; Yang C; Yang X; Lu Y; Luo Y; et al. PLoS One 2017, 12, No. e0175050. [PubMed: 28369094]

(40). Zhang P; He M; Zeng Y Lab Chip 2016, 16, 3033–3042. [PubMed: 27045543]

(41). Zhang P; Zhou X; He M; Shang Y; Tetlow AL; Godwin AK; Zeng Y Nat. Biomed. Eng 2019, 3, 438–451. [PubMed: 31123323]

(42). Beck TN; Boumber YA; Aggarwal C; Pei J; Thrash-Bingham C; Fittipaldi P; Vlasenkova R; Rao C; Borghaei H; Cristofanilli M; et al. BMC Cancer 2019, 19, 603. [PubMed: 31215484]

(43). Wu T-C; Xu K; Martinek J; Young RR; Banchereau R; George J; Turner J; Kim KI; Zurawski S; Wang X; et al. Cancer Res. 2018, 78, 5243–5258. [PubMed: 30012670]

(44). Vicentini C; Calore F; Nigita G; Fadda P; Simbolo M; Sperandio N; Luchini C; Lawlor RT; Croce CM; Corbo V; et al. BMC Gastroenterol. 2020, 20, 137. [PubMed: 32375666]

(45). Witek MA; Aufforth RD; Wang H; Kamande JW; Jackson JM; Pullagurla SR; Hupert ML; Usary J; Wysham WZ; Hilliard D; et al. npj Precis. Oncol 2017, 1, 24. [PubMed: 29657983]

(46). Wijerathne H; Witek MA; Jackson JM; Brown V; Hupert ML; Herrera K; Kramer C; Davidow AE; Li Y; Baird AE; et al. Commun. Biol 2020, 3, 613. [PubMed: 33106557]

(47). Soper SA; Ford SM; Qi S; McCarley RL; Kelly K; Murphy MC Anal. Chem 2000, 72, 642A–651A.

(48). Jackson JM; Witek MA; Hupert ML; Brady C; Pullagurla S; Kamande J; Aufforth RD; Tignanelli CJ; Torphy RJ; Yeh JJ; et al. Lab Chip 2014, 14, 106–117. [PubMed: 23900277]

(49). Jackson JM; Witek MA; Kamande JW; Soper SA Chem. Soc. Rev 2017, 46, 4245–4280. [PubMed: 28632258]

(50). Battle KN; Jackson JM; Witek MA; Hupert ML; Hunsucker SA; Armistead PM; Soper SA Analyst 2014, 139, 1355–1363. [PubMed: 24487280]

(51). Chang K-C; Hammer DA Biophys. J 1999, 76, 1280–1292. [PubMed: 10049312]

(52). Bell GI Science 1978, 200, 618–627. [PubMed: 347575]

(53). ONeil CE; Jackson JM; Shim S-H; Soper SA Anal. Chem 2016, 88, 3686–3696. [PubMed: 26927303]

(54). Im H; Shao H; Park YI; Peterson VM; Castro CM; Weissleder R; Lee H Nat. Biotechnol 2014, 32, 490–495. [PubMed: 24752081]

(55). Arraud N; Linares R; Tan S; Gounou C; Pasquet J-M; Mornet S; Brisson AR Haemostasis 2014, 12, 614–627.

(56). Dragovic RA; Gardiner C; Brooks AS; Tannetta DS; Ferguson DJP; Hole P; Carr B; Redman CWG; Harris AL; Dobson PJ; et al. Nanomedicine 2011, 7, 780–788. [PubMed: 21601655]

(57). Tong M; Brown OS; Stone PR; Cree LM; Chamley LW Placenta 2016, 38, 29–32. [PubMed: 26907379]

(58). Prat A; Karginova O; Parker JS; Fan C; He X; Bixby L; Harrell JC; Roman E; Adamo B; Troester M; et al. Breast Cancer Res. Treat 2013, 142, 237–255. [PubMed: 24162158]

(59). Uchiyama Y; Nakashima M; Watanabe S; Miyajima M; Taguri M; Miyatake S; Miyake N; Saitsu H; Mishima H; Kinoshita A; et al. Sci. Rep 2016, 6, 22985. [PubMed: 26957145]

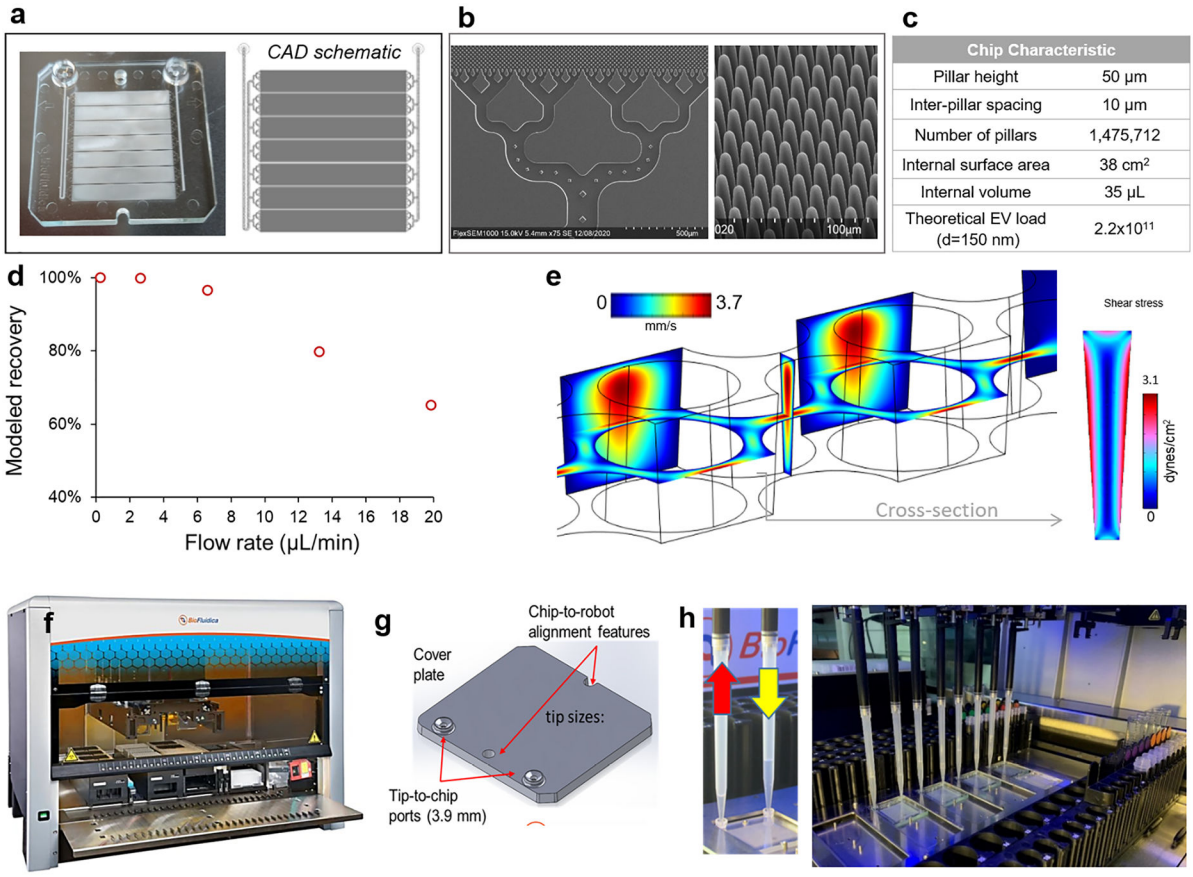

Figure 1.

(a) Micrograph and CAD design of a 7-bed EV-MAP device. (b) SEM images of the injection molded chip. (c) Dimensions of the EV-MAP device. The theoretical load was calculated by assuming an average EV size of 150 nm. (d) Recovery results as a function of flow rate from Monte Carlo simulations for the 7-bed EV-MAP design using 10 μm pillar spacing. (e) COMSOL Multiphysics simulation results showing 3D velocity cross-sections and shear stress profiles between two adjacent micropillars. Note the symmetry constraints placed along two sides of the simulation to achieve high element quality (Table S2) at a tractable computational cost. (f) Robotic platform for automated sample processing. The robot was based on a customized commercial system from Hamilton (Starlet). The robot could process up to 8 chips simultaneously. (g) Schematic showing the EV-MAP chip with its cover plate to accommodate insertion and operation by the robot. The chip, which measured 38 × 42 mm, was fitted with a COP cover plate containing conical ports to allow for leak-free interfacing to the pipette tips. (h) Pumping of the sample and reagents through the microfluidic architecture is achieved by the use of two pipetting channels simultaneously, one in push and one in pull mode.

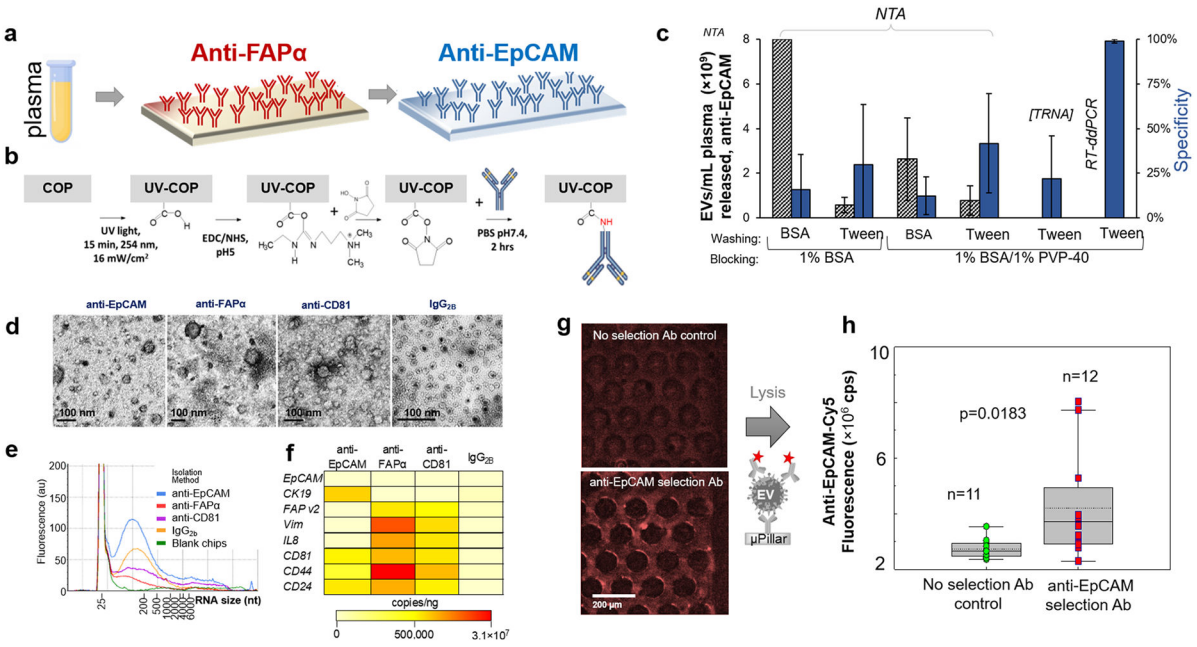

Figure 2.

(a) Affinity isolation of EVs performed in a serial fashion. (b) Schematic of a direct attachment of mAb to the surface of a UV/ozone activated polymer surface. (c) Optimization of blocking and washing buffers based on maximizing specificity achieved from healthy donor plasma samples. Specificity was calculated based on subtraction of the nonspecific IgG2B EV NP concentrations from the anti-EpCAM EV concentrations and dividing by the total number of nanoparticles collected as measured through NTA. Comparison of assay specificity is also included based on NTA results, RNA quantification, and mRNA copy quantification. (d) TEM images of EV fractions isolated from the donor plasma sample, with the same sample also used to extract total RNA for RT–ddPCR analysis. (e) Total RNA for each EV fraction analyzed using high-sensitivity RNA tape. The total RNA concentration generated per isolate ranged from 706 pg/μL (anti-EpCAM isolate) to 155 pg/μL (anti-FAPα isolate). (f) 2 μL of the total RNA was used for RT–ddPCR. The total copy results were normalized to the ng of the total RNA input into RT. (g) Fluorescent images of a negative control (no mAb attached to the surface of a pristine chip) and positive control (anti-EpCAM antibody covalently attached to the chip surface) collected after SKBR3 cell line-conditioned medium was processed through the anti-EpCAM EV-MAP chip and stained with anti-EpCAM–Cy5 mAb. (h) Following affinity isolation and staining, the material within the device was lysed in both negative and positive controls, and samples' fluorescence was measured using a fluorescence spectrometer.

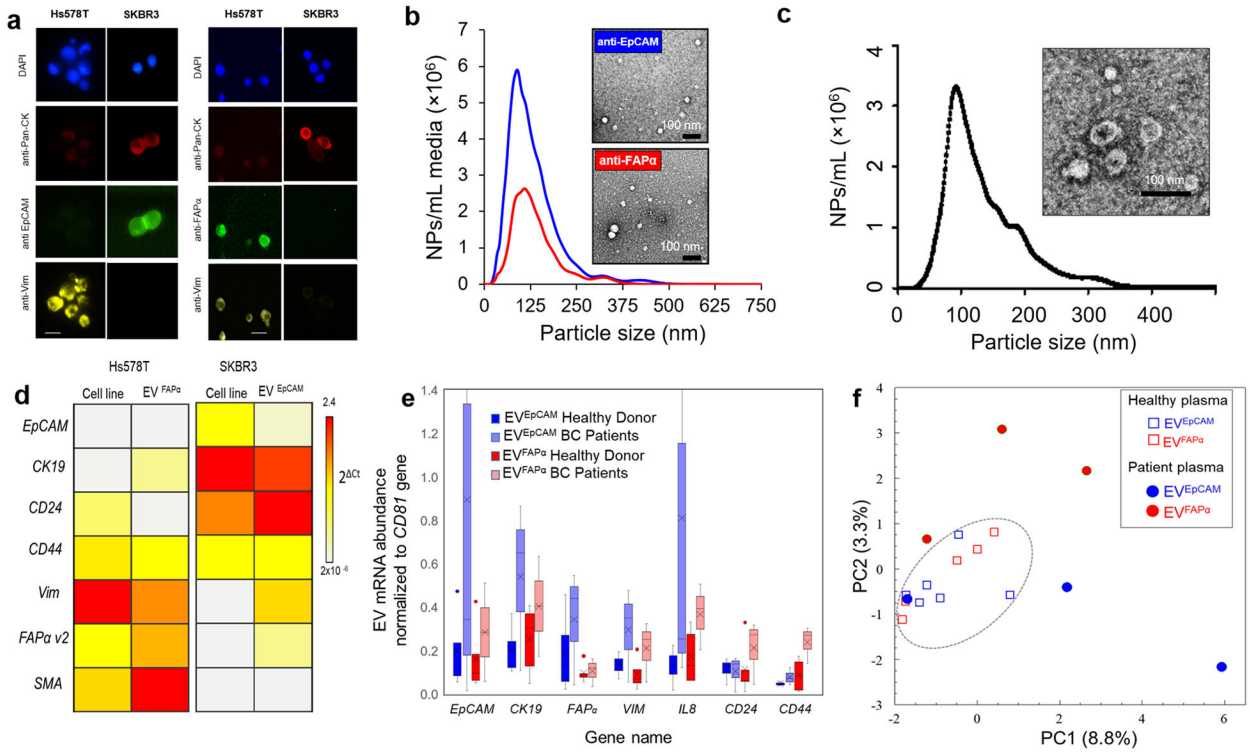

Figure 3.

(a) Immunophenotyping of SKBR3 and Hs578T BC cell lines for several protein markers including Pan-CK, EpCAM, FAPα, and vimentin as well as nuclear staining with DAPI, (scale bar = 20 μm). (b) NTA data for EV^{EpCAM} and $EV^{FAP\alpha}$ isolated from SKBR3 and Hs578T conditioned cell media and examples of TEMs, and (c) SKBR3 EVs isolated via ultracentrifugation and a TEM image collected for these EVs. (d) RT-qPCR mRNA gene profiles of SKBR3 and Hs578T cells and their respective EVs. EVs were isolated from conditioned media by the EV-MAP device. (e) EV^{EpCAM} and $EV^{FAP\alpha}$ mRNA abundance for healthy donors and BC patients. (f) PCA of analyzed mRNA from EV^{EpCAM} and $EV^{FAP\alpha}$ isolated from healthy donor plasma and BC patients, and blue and red text indicates EV^{EpCAM} and $EV^{FAP\alpha}$ subpopulations, respectively. Data for BC patients are irrespective of the subtype or receptor status of the cancer.

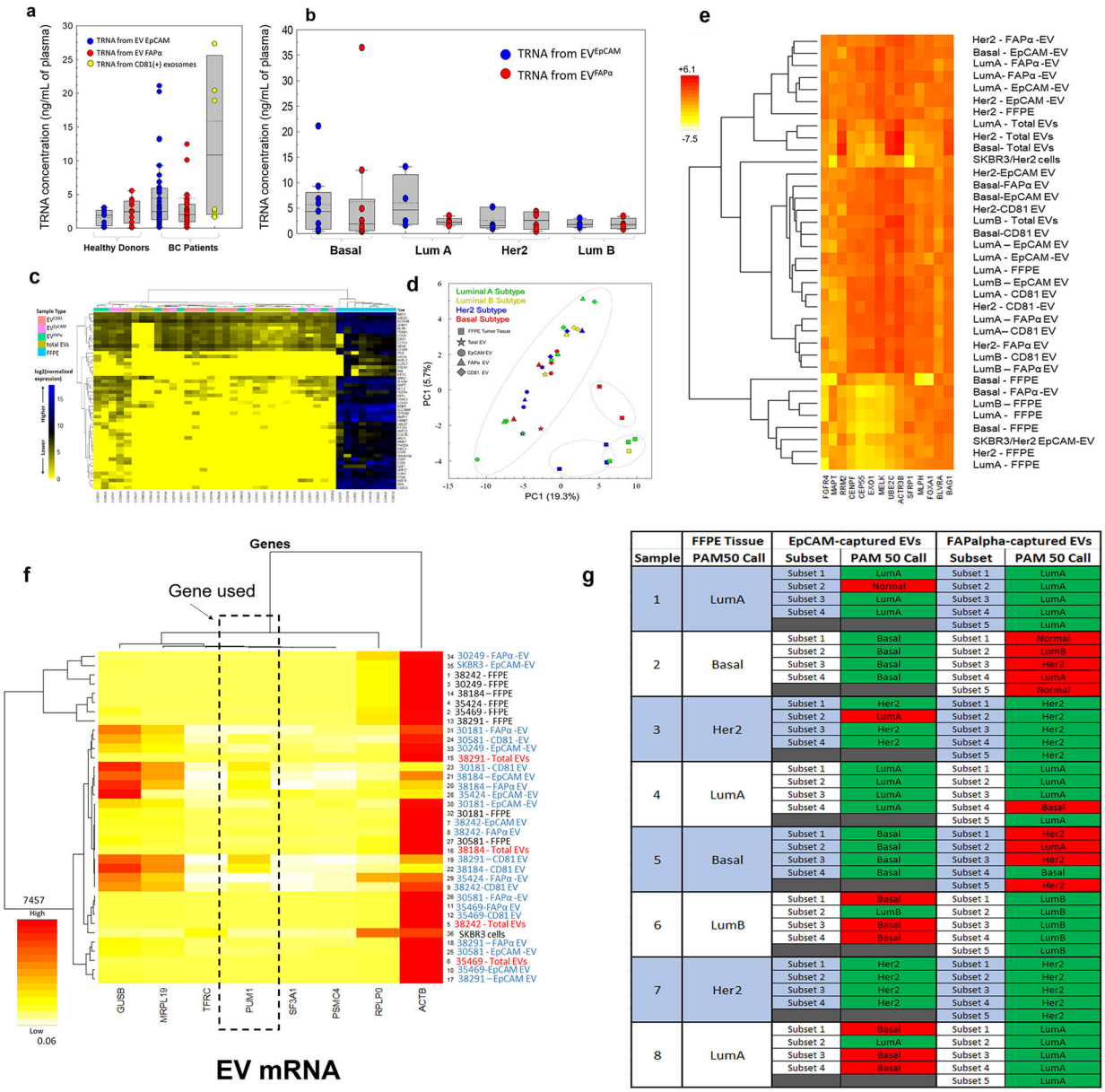

Sample	FFPE Tissue PAM50 Call	EpCAM-captured EVs Subset	EpCAM-captured EVs PAM 50 Call	FAPalpha-captured EVs Subset	FAPalpha-captured EVs PAM 50 Call
1	LumA	Subset 1	LumA	Subset 1	LumA
		Subset 2	Normal	Subset 2	LumA
		Subset 3	LumA	Subset 3	LumA
		Subset 4	LumA	Subset 4	LumA
				Subset 5	LumA
2	Basal	Subset 1	Basal	Subset 1	Normal
		Subset 2	Basal	Subset 2	LumB
		Subset 3	Basal	Subset 3	Her2
		Subset 4	Basal	Subset 4	LumA
				Subset 5	Normal
3	Her2	Subset 1	Her2	Subset 1	Her2
		Subset 2	LumA	Subset 2	Her2
		Subset 3	Her2	Subset 3	Her2
		Subset 4	Her2	Subset 4	Her2
				Subset 5	Her2
4	LumA	Subset 1	LumA	Subset 1	LumA
		Subset 2	LumA	Subset 2	LumA
		Subset 3	LumA	Subset 3	LumA
		Subset 4	LumA	Subset 4	Basal
				Subset 5	LumA
5	Basal	Subset 1	Basal	Subset 1	Her2
		Subset 2	Basal	Subset 2	LumA
		Subset 3	Basal	Subset 3	Her2
		Subset 4	Basal	Subset 4	Basal
				Subset 5	Her2
6	LumB	Subset 1	Basal	Subset 1	LumB
		Subset 2	LumB	Subset 2	LumB
		Subset 3	Basal	Subset 3	LumB
		Subset 4	Basal	Subset 4	LumB
				Subset 5	LumB
7	Her2	Subset 1	Her2	Subset 1	Her2
		Subset 2	Her2	Subset 2	Her2
		Subset 3	Her2	Subset 3	Her2
		Subset 4	Her2	Subset 4	Her2
				Subset 5	Her2
8	LumA	Subset 1	Basal	Subset 1	LumA
		Subset 2	LumA	Subset 2	LumA
		Subset 3	Basal	Subset 3	LumA
		Subset 4	Basal	Subset 4	LumA
				Subset 5	LumA

Figure 4.

(a) Box plots presenting the concentration of total RNA extracted from isolated EV^{EpCAM} and $EV^{FAP\alpha}$ from healthy donors and BC patients' plasma. (b) Concentration of total RNA extracted from isolated EV^{EpCAM} and $EV^{FAP\alpha}$ separated by the subtype of the primary tumor tissue at the time of diagnosis. (c) EV mRNA analysis using PAM50 test. Heatmaps for 50 panel gene and BC samples. Total EVs, affinity-isolated CD81(+) EVs, and FAPα(+) or EpCAM(+) EVs were selected from BC plasma samples and tested with PAM50. (d) PCA was performed on analyzed samples and clearly distinguished EVs from tissue BC mRNA. (e) Heatmap showing the expression pattern of exo-mRNA in different plasma samples analyzed in this study. Also shown are the expression patterns for the mRNA harvested from FFPE tissue. For the exo-mRNA, the EVs were affinity-selected from the plasma samples using the EV-MAP chip and the EVs were lysed followed by solid-phase extraction of

the total RNA. For the FFPE samples, the tissue was lysed and subjected to solid-phase extraction. In both cases, the solid-phase-extracted total RNA was subjected to the nCounter assay. (f) Heat map composed from log2 Prosigna mRNA counts and normalized to *PUM1* reference gene. (g) Identification of breast cancer molecular subtype based on PAM50 profiling using mRNA isolated from EV^{EpCAM} and $EV^{FAP\alpha}$ for diffident BC subtypes.